


RESEARCH

Open Access



Ultracompact multifunctional metalens visor for augmented reality displays

Yan Li^{1†}, Shuyi Chen^{1†}, Haowen Liang^{2*}, Xiuying Ren¹, Lingcong Luo², Yuye Ling¹, Shuxin Liu¹, Yikai Su^{1*} and Shin-Tson Wu^{3*} 

[†]Yan Li and Shuyi Chen contributed equally to this work.

*Correspondence: lianghw26@mail.sysu.edu.cn; yikaisu@sjtu.edu.cn; swu@creol.ucf.edu

¹ Department of Electronic Engineering, Shanghai Jiao Tong University, Shanghai 200240, China

² State Key Laboratory of Optoelectronic Materials and Technologies, School of Physics, Sun Yat-Sen University, Guangzhou 510275, China

³ College of Optics and Photonics, University of Central Florida, Orlando, FL 32816, USA

Abstract

Virtual reality (VR) and augmented reality (AR) have found widespread applications in education, engineering, healthcare, and entertainment. However, these near-eye displays are often bulky and heavy, and thus are not suitable for long-term wearing. Metalenses, with an ultra-thin formfactor, subwavelength modulation scale, and high modulation flexibility, are promising candidates to replace the conventional optics in AR display systems. In this work, we proposed and fabricated a novel reflective dielectric metalens-visor based on Pancharatnam-Berry phase with see-through capability. It achieves diffraction-limited focusing behavior for the reflected red light, while keeping a good transmission spectrum in the visible region. Hence, this single piece metalens-visor can perform the function of two integrated elements simultaneously: an eyepiece and an optical combiner, which in turn greatly reduces the weight and the size of an AR display. We have implemented a proof-of-concept AR display system employing the metalens-visor, and experimentally demonstrated color AR images with good image quality. This work reveals the great potential of multi-functional metasurface devices which enables optical integration in interdisciplinary applications including wearable displays, biological imaging, and aeronautic optical instruments.

Keywords: Metalens-visor, Wearable display, Augmented reality, See-through metasurface, Multi-functional

Introduction

Recently, virtual reality (VR) and augmented reality (AR) are revolutionizing the way we perceive and interact with the world [1–4]. Their widespread applications include but are not limited to healthcare, education, entertainment, and military training. While VR is immersive, AR enables users to see both the digital information and the surrounding real world [5]. To reduce the weight and volume of VR and AR headsets, compact optical elements are in urgent need.

Metasurfaces are ultra-thin planar elements that could overcome the limitations of refractive optics and conventional diffractive optics. They can precisely control the wavefront of light via subwavelength structures with high degrees of freedom. Various metasurface devices, such as gratings [6–9], lenses [10–12], holograms [13–19], and optical vortex plates [20–22], have been developed to realize versatile functionalities.

Metalenses, which can realize light focusing within an ultra-compact dimension, have opened up a wide range of applications including imaging [23–28], sensing [29] and spectroscopy [30, 31] and have been extensively studied [32]. Recently, the materials used for fabricating metalenses have been extended from metals to all-dielectric. Metal metalenses usually suffer from low transmission efficiency due to their strong intrinsic absorption in the visible region, while all-dielectric metalenses are gaining ever-increasing research attention with high transparency.

With their ultra-thin formfactor, subwavelength modulation scale and high modulation flexibility, metalenses have been suggested as key components in near-eye visors targeted for AR and VR applications. In 2018, Lee et al. [24] employed a large-area transmissive dielectric metasurface as an eyepiece in an AR system. Li et al. [2] designed and fabricated a transmissive red-green-blue-achromatic metalens, and demonstrated a compact VR system based on it. Wang et al. [33] proposed a 5-mm diameter metalens eyepiece composed of silicon nitride nanofins, and employed it in a 3D holographic near-eye display. In 2022, Li et al. [34] demonstrated a large-scale metalens using a general inverse-design framework and set up a VR platform based on this meta-eyepiece. The abovementioned transmissive metalenses are strong contenders as ultrathin eyepieces. However, if such transmissive metalenses are to be used in an optically see-through AR system, an additional optical combiner is required to merge the virtual images with the real scenes. And that would add up to the complexity, weight or formfactor of the AR systems. Figure 1a shows the schematic diagram of a near-eye AR display system employing a transmissive metalens and a beam splitter combiner.

Recently, compact near-eye display schemes based on reflective metalenses have also been proposed. Hong et al. [35] designed a flat reflective off-axis dielectric metalens to replace the geometric freeform lens in a near-eye display, and Bayati et al. [36] reported simulation work on the design of a see-through AR visor based on composite metasurfaces; but they only provided verification by simulation and did not build prototypes to experimentally evaluate the actual imaging performance. Avayu et al. [37] proposed an early form of see-through metalens-visor with three metallic layers, and Nikolov et al. [38] also demonstrated a reflective optical surface that combines the benefits of a free-form optic and a metasurface for AR/VR displays. However, the see-through capability

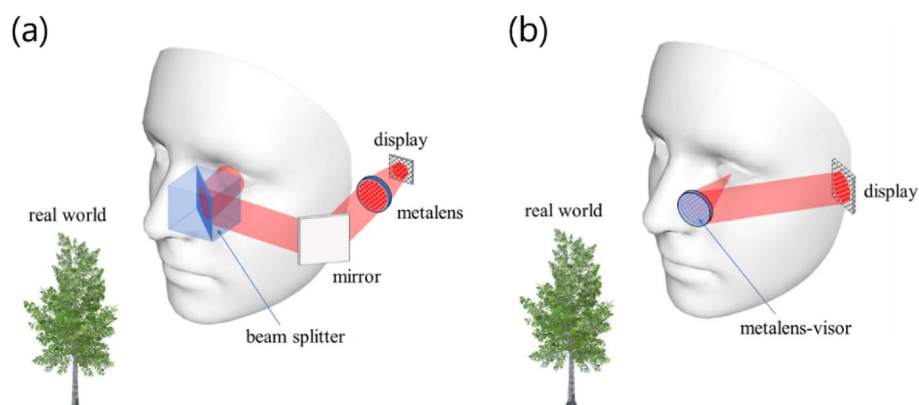


Fig. 1 Simplified schematic diagrams of near-eye AR display systems based on (a) a traditional transmissive metalens and (b) a single piece see-through reflective metalens-visor

and AR imaging effect of these approaches are yet to be demonstrated. Song et al. [39] established a see-through non-local metasurface that provides high transparency in the visible region; but it could only diffract reflected near-infrared (NIR) light instead of visible light, for the purpose of eye tracking; thus it could not function as an AR imaging visor. To the best of our knowledge, the optical see-through AR imaging effect using a single piece metalens-visor has not been experimentally demonstrated before.

In this paper, we propose and experimentally demonstrate an optical see-through reflective dielectric metalens, that is capable of reflecting and focusing off-axis visible light while preserving a good see-through property, for the first time. Such a metalens could simultaneously function as an off-axis eyepiece and an optical combiner in an AR display system, as shown in Fig. 1b. Hence, it can immensely reduce the complexity, formfactor and weight of the near-eye AR system, and thus improve the comfort and immersion experience for users. We have achieved a diffraction limited focal spot with a reasonably high efficiency at $\lambda = 633$ nm and obtained good transmission spectrum covering the range from 400 nm to 700 nm. The experimental results agree very well with simulation. With the proposed metalens-visor, we have implemented a proof-of-concept AR display system, and experimentally demonstrated color virtual images with good image quality augmented on the real world. We believe the development of this ultrathin metalens with such attractive optical properties would pave the way towards realizing next-generation compact displays for AR applications.

Results

Figure 2a shows the schematic illustration of the optical behavior of the proposed see-through reflective metalens. Different from conventional metalenses, our metalens is optimized to achieve good focusing effect for the 45° incident light while maintaining a good transmission spectrum for the normal incidence. The collimated oblique incident light is reflected towards the normal direction while being converged by the metalens, which functions like an off-axis reflective lens. To realize such an optical behavior, the phase profile $\phi(x, y)$ of the metalens should be designed as (see Supplementary S1 and Fig. S1 for the detailed derivation):

$$\phi(x, y) = \frac{2\pi}{\lambda_d} \left(f - \sqrt{x^2 + y^2 + f^2} - \frac{x}{\sqrt{2}} \right) \quad (1)$$

where x and y are the coordinates of each unit cell, λ_d is the design wavelength, and f is the focal length. To realize such phase distribution, we designed a Pancharatnam-Berry (PB) phase metalens, whose unit cell structure is shown in Fig. 2b. It consists of a crystalline silicon (Si) nanofin on a sapphire substrate with fixed length L , width W , height H , and period P , but spatial-varying rotation angle $\theta(x, y)$. For a circularly polarized incident light, the rotation angle of each nanofin generates a phase shift $\phi(x, y) = 2\theta(x, y)$, which is caused by the birefringence arising from the asymmetric nanofin structure [40, 41]. Therefore, the desired deflection and focusing effects can be achieved.

In the design and optimization of this optical see-through reflective metalens-visor, both reflection (for the virtual images) and transmittance (for the environmental scenes) conditions should be considered. First, according to Fresnel theory, to achieve high reflection, it is important to have high refractive index contrast at the interface. Silicon

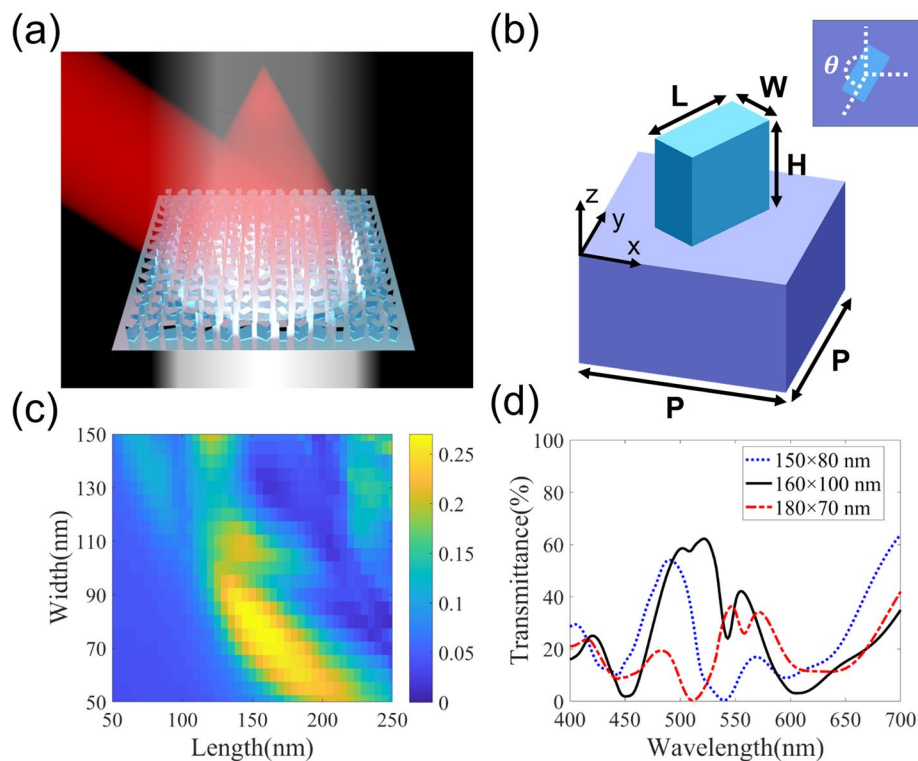


Fig. 2 Schematics of the metalens. **(a)** Schematic illustration of the optical behavior of the proposed see-through reflective metalens. **(b)** Schematic illustration of a unit cell of the metalens, consisting of a Si nanofin on the sapphire substrate with fixed length L , width W , height H , and period P , but varying rotation angle θ according to the Pancharatnam-Berry phase. **(c)** 1st order diffraction efficiencies of the reflected light, as the length and width of the nanofins vary while the height is fixed to be 230 nm. **(d)** 0th order transmission spectra of the meta-grating-cell, with the corresponding length \times width of each nanofin labeled in the legends

is a high refractive index material, that is compatible with the process of Complementary Metal Oxide Semiconductor (CMOS) mass production and industrialization, and it has already been used for realizing high performance metalenses [24, 42–44]. Compared to amorphous silicon, crystalline silicon has a lower absorption coefficient in the visible wavelengths and has been reported to be a material platform for high efficiency metalenses [45–47]. Second, to preserve a good see-through property, the size of the nanofin and the filling ratio of the unit cell are critical due to the non-negligible absorption of silicon in the visible region [46, 48], and therefore need to be subtly tuned. Third, to achieve high diffraction efficiency for the reflected light, it is desired that the orthogonal polarization components to experience similar amplitude attenuation but a phase retardation close to π upon reflection, according to the PB phase. Therefore, we conducted systematic simulations to optimize the structure parameters using a commercial finite-difference time-domain (FDTD) solver (Lumerical Inc., Vancouver). We varied the length, width, and height of the nanofins in a meta-grating-cell with six gray levels (Fig. S2), trying to obtain high 1st order diffraction efficiency in reflection and balanced transmission spectra for the normal incident light covering from 400 nm to 700 nm. Detailed optimization process is described in Supplementary S2, and the simulated results are shown in Fig. S3. Figure 2c shows the 1st order diffraction efficiencies of the reflected

light, as the length and width of the nanofins vary while the height is kept at 230 nm. And Fig. 2d shows the simulated transmission spectra for three selected groups of structures. After balancing the reflection and transmission performance, we decided the optimized parameters of the metalens are $P=250$ nm, $L=160$ nm, $W=100$ nm, and $H=230$ nm.

As shown in Fig. 1b, which is the schematic illustration of an AR eyeglasses architecture using the proposed metalens visor, an off-axis incident image from the microdisplay is reflected and converged by the metalens towards the eye pupil. Meanwhile, due to the see-through capability of the visor in the visible region, ambient natural light can directly pass through and then enter the eye. Hence, the eye can see virtual images augmented on the real world through the ultra-compact single piece visor.

To validate our design, we fabricated a metalens at the design wavelength of $\lambda_d=633$ nm. Figure 3 shows the scanning electron microscope (SEM, Zeiss Auriga) images of a fabricated sample. Figure 3a shows the top-view of the central portion of the metalens, and Fig. 3b shows the sidewalls of the nanofins through a 45° tilted-view. From the figures, we find that the structure parameters of these nanofins agree well with the design values. Because of fabrication imperfection, the nanofins are not strictly rectangular, but with some rounded corners. Thanks to the large tolerance of PB phase [49], such rounded corners, however, have little influence on the performance of PB metalenses except for a slight efficiency variation. It should be noted that, because of our limited fabrication facility, the sample possesses a smaller area of 1×1 mm² (4000×4000 units), resulting in a smaller numerical aperture (NA) of 0.035 (see Supplementary S3 and Fig. S5 for the detailed characteristic parameter description). Here, the NA of the metalens is calculated based on the diagonal of the square aperture.

We first characterized the focusing performance of our reflective metalens using a HeNe laser beam (633 nm). At about 20-mm away from the metalens in the normal reflection direction, we observed the minimal focal spot on a screen, which confirms the realization of a focal length of approximately 20 mm. To precisely measure the focal spot size, we adopted the experimental setup depicted in Fig. S6, and the focal spot image captured by a charge-coupled device (CCD) camera is shown in Fig. 4. Figure 4a to 4c shows the measured symmetric focal spots of our metalens at three discrete illumination wavelengths, including the design wavelength of 633 nm and another two specific wavelengths of 532 nm and 457 nm. The corresponding cross-sections of the three focal spots are shown in Fig. 4d to 4f with the full width at half maximum (FWHM) labeled in the

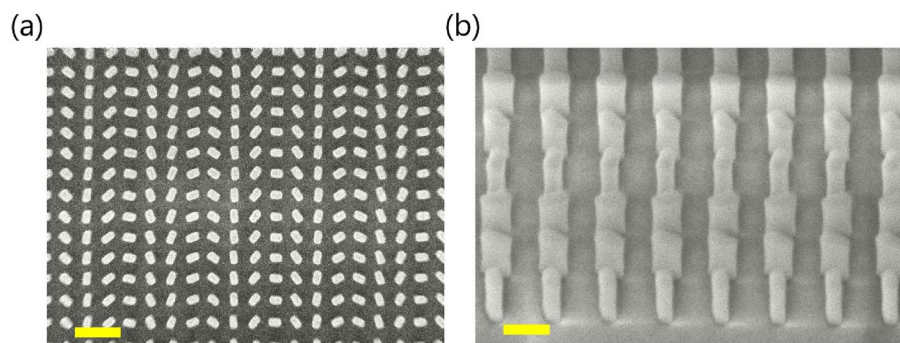


Fig. 3 Scanning electron micrographs of the fabricated metalens. **(a)** Top-view of the central section of the metalens. Scale bar = 400 nm. **(b)** Tilted-view (45°) of a portion of the metalens. Scale bar = 200 nm

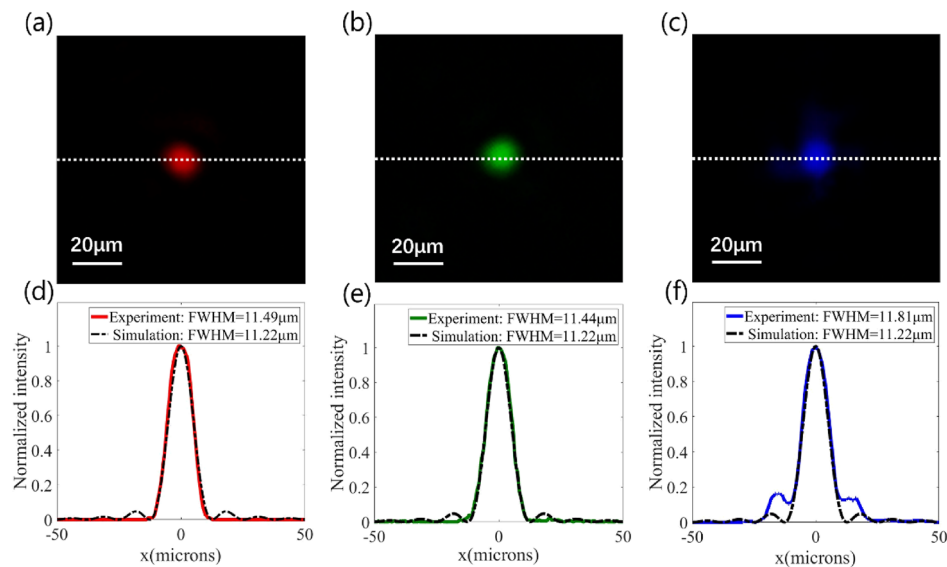


Fig. 4 Focal spots of the fabricated metalens with $NA = 0.035$ at RGB illumination and comparison with simulation results. **(a to c)** Measured focal spot intensity profile at the illumination wavelengths of **(a)** 633 nm, **(b)** 532 nm and **(c)** 457 nm. **(d to f)** Corresponding normalized intensity profiles along the white dashed lines in **(a to c)** respectively and comparison with simulation results based on Rayleigh-Sommerfeld diffraction. FWHMs of both the experimental and simulated results are labeled in the legends

legends. The metalens shows slight defocusing at the illumination of blue light (Fig. 4f) because the phase mask is designed for $\lambda = 633$ nm instead of 457 nm. We also simulated the focusing properties based on the Rayleigh-Sommerfeld diffraction formulas in Matlab and obtained the cross-sections of focal spots at the three wavelengths with the corresponding FWHM labeled in the legends (Fig. 4d to 4f). The focal spots of our metalens at the three illumination wavelengths are near diffraction limited. Although the metalens is designed for $\lambda = 633$ nm, it presents good focusing performance for all the red, green, and blue colors. Fig. S8 shows the enlarged focal spot of the fabricated metalens at the illumination wavelength of 633 nm, compared with the simulation results in FDTD. We further measured the focusing efficiencies of our fabricated metalens with a detector (Newport 918D-SL-OD3) placed right at the focal plane in front of the metalens. Here the focusing efficiency is defined as the ratio of power of light collected by the detector at the focal plane to that of the circularly polarized incident light. The measured focusing efficiencies are 16.03%, 3.92% and 2.01% at $\lambda = 633$ nm, 532 nm, and 457 nm, respectively. The efficiency for red light incidence is quite competitive according to ref. [24], ref. [39] and ref. [50]. The relatively low efficiencies for green and blue are mainly attributed to the unoptimized unit cell structure for these two wavelengths, as well as stronger absorption of the silicon material at shorter wavelengths.

We also measured the visible transmission spectrum of the metalens using a spectrometer, and the light source was also set to be right-handed circularly polarized. As shown in Fig. 5, one could see that the metalens possesses good see-through characteristics with a relatively high efficiency for most of the visible light. The simulation curve in Fig. 5 is obtained for a downsized metalens with a small aperture of $7.5 \times 7.5 \mu\text{m}^2$ (30×30 units) while keeping the same NA of 0.035 as the fabricated one. Overall, the experimental result is in good agreement with simulation, except that the dips in the

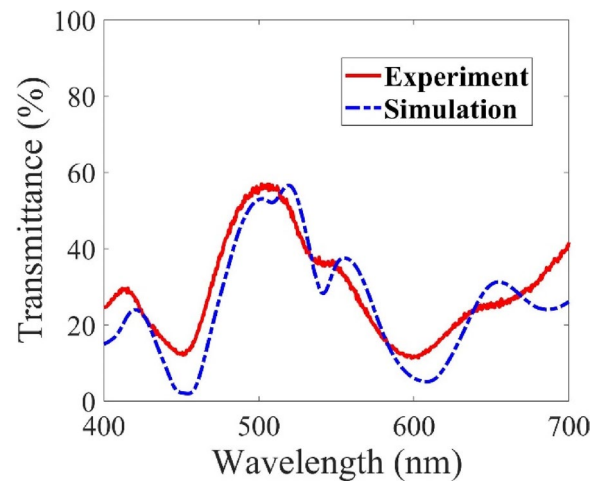


Fig. 5 Transmission characterization of the fabricated metalens. Comparison of simulated and measured transmittance spectra of the metalens

measured spectrum seem to be shallower than expected. Such a deviation might be attributed to the measurement errors or fabrication imperfection. For instance, although we attached a diaphragm aperture with a diameter of 0.8 mm to the sample, trying to prevent the incident light from reaching beyond the effective region ($1\text{ mm} \times 1\text{ mm}$), there might still be some unwanted stray light entering outside the effective region due to imprecise alignment. In addition, we also carried out simulation to verify that our metalens barely generates transmitted wavefront distortion of a plane wave (see Supplementary S5 for detailed description).

Thanks to its good see-through property and focusing performance, we employed the fabricated metalens-visor in a prototype of an AR display where it performs the function of an eyepiece and a combiner simultaneously. Figure 6 shows the experimental setup for realizing the AR display system. Illuminated by collimated laser light, the reflective spatial light modulator (SLM) generates the desired virtual image pattern for the AR display. After passing through a circular polarizer, the virtual image light is converted to right-handed circular polarization. Then a telescope system consisting of two positive

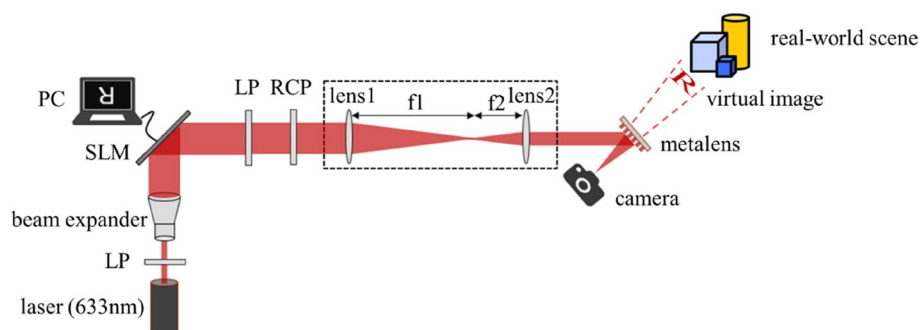


Fig. 6 Illustration of the optical setup for the AR imaging system. LP denotes a linear polarizer and RCP denotes a right-handed circular polarizer, SLM is the spatial light modulator (Jasper Q4K70) and PC is a personal computer. A camera is used to imitate human eye. The black dashed box indicates the telescope system, which is used to downsize the virtual image

lenses (lens1: $f=400$ mm; lens2: $f=50$ mm) is used to reduce the beam size while maintaining its collimated nature, so that the output light with a reduced beam size only illuminates the effective region of the sample. Next, careful orientation adjustment of the sample is performed, to assure the beam impinging on the sample with an incident angle of 45° . If the human eye is positioned at the focal point, it should be able to see both the reflected virtual image and the real-world scene. In our experiment, we used a camera (CANON EOS M10 with CANON ZOOM LENS EF-M 15–45 mm) to replace the human eye to capture the displayed images. Here, a black card with a $1\text{ mm} \times 1\text{ mm}$ hole was also affixed on the back of the sample, and strictly aligned with it, to make sure that the effective region is the only window that the real-world light could pass through.

Figure 7a to 7c shows the AR imaging results when the camera was focused at different distances. In the figures, one can see the augmentation of a virtual image “R” on the real-world scene that has three representative real objects, a dial, a puppet, and a piece of white paper with black letters “SJTU” printed on it, placed at 150 mm, 600 mm, and 2000 mm away from the camera, respectively. The quality of the virtual image is reasonably good, except for some noise due to the diffraction effect caused by the small pixel size ($3.74\ \mu\text{m}$) of the SLM (Jasper Q4K70) and the coherent laser light employed. This problem can be alleviated by optimizing the distance between the telescope system and the metalens-visor, and by choosing other image sources such as a laser scanning projector [51]. Employing a narrowband light-emitting diode (LED) light source could also help improve the image quality, as diffraction effect and speckle noise could be suppressed due to its low coherence. The real-world scene is clearly seen with high color fidelity. So indeed, the proposed single-piece metalens-visor could realize the functions of a reflective lens and an optical combiner simultaneously. Such a metalens-visor would undoubtedly decrease the system complexity, weight, and formfactor of an AR display, which are critical for the comfortable wearing of an AR headset.

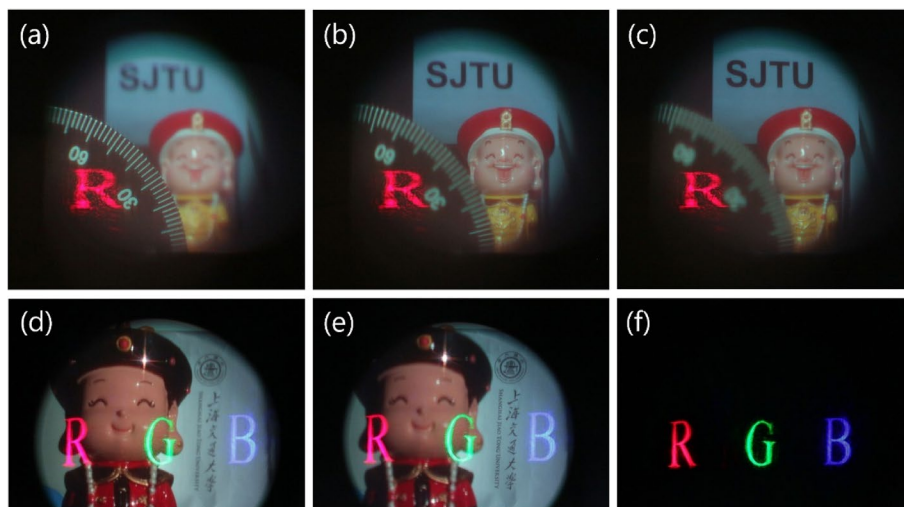


Fig. 7 Imaging results of the metalens-visor. **(a to c)** Demonstration of single-color AR imaging under red (633 nm) laser illumination. The images are focused at **(a)** 150 mm (dial), **(b)** 600 mm (puppet) and **(c)** 2000 mm (“SJTU”), respectively. **(d, e)** Demonstration of multi-color AR and **(f)** corresponding VR imaging under red (633 nm), green (532 nm) and blue (457 nm) laser illumination. The images are focused at **(d)** 200 mm (puppet) and **(e)** 1200 mm (logo and texts), respectively. The real objects will become blurry or clear as the focus changes, while the virtual images are always clear due to the Maxwellian View display technique

Moreover, because a collimated virtual-image light was employed in our experiment, an interesting phenomenon was observed. As shown in Fig. 7a, when the camera was focused at the depth of the dial (150 mm), the virtual image “R” was clearly displayed but the distant puppet and “SJTU” are blurred. In Fig. 7b and c, when the camera was focused at the depth of the puppet (600 mm) and “SJTU” (2000 mm), respectively, the virtual image was always clear. We observed the similar phenomenon when we used a black scattering screen to receive the real images employing the experimental setup shown in Fig. S10, and Fig. S11 shows the corresponding imaging results. We also used a receiving screen with graduated scale to measure the image size at different depths. As shown in Fig. S12, the image size decreases first and then increases. And the minimum image size (a point) was achieved right at the focal length of our metalens. Thus, the collimated image light is converged into a point by the metalens visor. If the pupil is positioned at the focal point, it would be like a pinhole imaging system, and allow the user to observe always-clear images on the retina regardless of eye accommodation. Such a display technique employed here is the Maxwellian View display technique [52] (see Supplementary S7 and Fig. S13 for more detailed explanation). Maxwellian-view display is one of the effective approaches to overcome the vergence-accommodation conflict, which induces 3D visual fatigue in conventional AR displays [53, 54]. Other display technologies including holographic display [55, 56], super-multi-view display [57, 58] and volumetric display [59, 60] can also help to alleviate this problem. Maxwellian-view display is simple to implement, but it suffers from having a small eyebox, which makes the virtual image easily missed out as the eye moves. Possible solutions to address this problem include employing multi-view display technique [58] or pupil duplication technique [61, 62] as described in the Supplementary S8 and shown in Fig. S14.

As discussed before, the reflective metalens-visor possesses good focusing characteristics for green (532 nm) and blue (457 nm) wavelengths as well, although it is designed for a single wavelength of 633 nm. Thus, we further employed red, green and blue lasers (633 nm, 532 nm and 457 nm) as the light sources for the AR display, to perform RGB color imaging. Theoretically, if the metalens-visor is achromatic, we could conveniently realize full color imaging by strictly aligning red, green and blue beams as shown in Fig. S15. Taking the dispersive nature of our metalens-visor into consideration, which yields distinctively different diffraction angles for 532 nm and 457 nm, we carefully adjusted the incident angles and divergence of the three beams (see Fig. S16 for experimental setup), so that the red (letter “R”), green (letter “G”) and blue (letter “B”) virtual images can be captured by the camera simultaneously. Figure 7d and e, shows the multi-color AR images at different focusing distances, and Fig. 7f shows the corresponding VR image for the same virtual content. Similarly, one can see in Fig. 7d and e, the virtual images are always clear as the camera’s focus distance varies. The bright spot in the figure is the light reflected from the puppet’s smooth surface when the real-world background is illuminated with a desk lamp. Here, the virtual image quality is improved because diffraction is suppressed by replacing the pixelated SLM with 3 patterned masks to generate red, green, and blue images. The feature size of the patterned masks is 8 mm × 5 mm. And they are commercial photomasks made of polyester materials by laser drilling.

Here, because of the polarization dependency of the PB metalens, an additional circular polarizer (a linear polarizer + a quarter-wave plate) is required to generate a circularly polarized incidence light from our linearly polarized laser beam. But the addition of such an ultrathin circular polarizer would barely increase the energy loss, weight, or cost of the system.

In Fig. 7, the transmitted real-world scene perseveres quite good color characteristics except for being a little bit more greenish than the actual scene. The greenish color is due to the relatively high transmittance of the metalens in the green band than those in the red and blue bands, as shown in Fig. 5. To improve color fidelity, the transmission spectrum of the metalens could be further optimized to achieve a more balanced transmittance for the RGB bands.

Discussion

It is evident from the experiment that the virtual images can be augmented on the real-world scene by a single-piece metalens-visor. At the current stage, because the fabricated metalens possesses a small NA, the AR display prototype has a limited field of view (FOV). The calculation of FOV is presented in the Supplementary S3 and shown in Fig. S5. To achieve a large field of view (FOV) in an AR display, high NA is required for the metalens. For instance, to realize a 93° diagonal FOV (74° horizontally and 74° vertically), the NA of the metalens needs to be 0.73. Thus, for a metalens with a focal length of 15 mm, which provides a reasonably large eye clearance, its aperture should be $22.5 \times 22.5 \text{ mm}^2$. We also simulate such a metalens with large NA (0.73). In the simulation, we downsized the area of the target metalens to $7.5 \times 7.5 \mu\text{m}^2$ (30×30 units) and its focal length to $5 \mu\text{m}$, so that the NA and focusing performance of the metalens could be kept the same. Figure 8a shows the simulated normalized light intensity profile at the focal plane ($z = 5 \mu\text{m}$) of the metalens and Fig. 8b shows the corresponding normalized intensity profile along the red dashed lines in Fig. 8a. The FWHM of the focal spot is $\sim 492 \text{ nm}$, which is relatively close to the diffraction limit. Figure 8c and d shows the normalized intensity distribution in the x - z plane and y - z plane, respectively. One can see that indeed the focal point is located approximately at $z = 5 \mu\text{m}$, which is consistent with the theoretical value. Furthermore, the depth of focus is about $2 \mu\text{m}$; the focusing efficiency reaches 16.7%, which is higher than previous reported metallic and polycrystalline silicon-based strategies [23, 24]. This reflective metalens demonstrates good focusing properties for the oblique incident light, maintaining good see-through characteristics in the visible band at the same time. With advanced fabrication methods such as nanoimprint [24] and stepper lithography [63], it is possible to fabricate metalenses with a larger area and NA, enabling a larger FOV in AR displays.

Despite the dispersion characteristics, we also successfully demonstrated red, green, and blue color imaging using the metalens-visor, while being able to see through the real world without obvious distortion or color infidelity. Although the chromatic aberration has always been an inherent limitation of metasurfaces, it can be corrected through multiple methods, such as compound achromatic metalens with multilayer structure [23, 37], compensation by refractive optics [64], separate engineering of phase, group-delay and group-delay-dispersion [28, 65] or other techniques based on coupled resonances

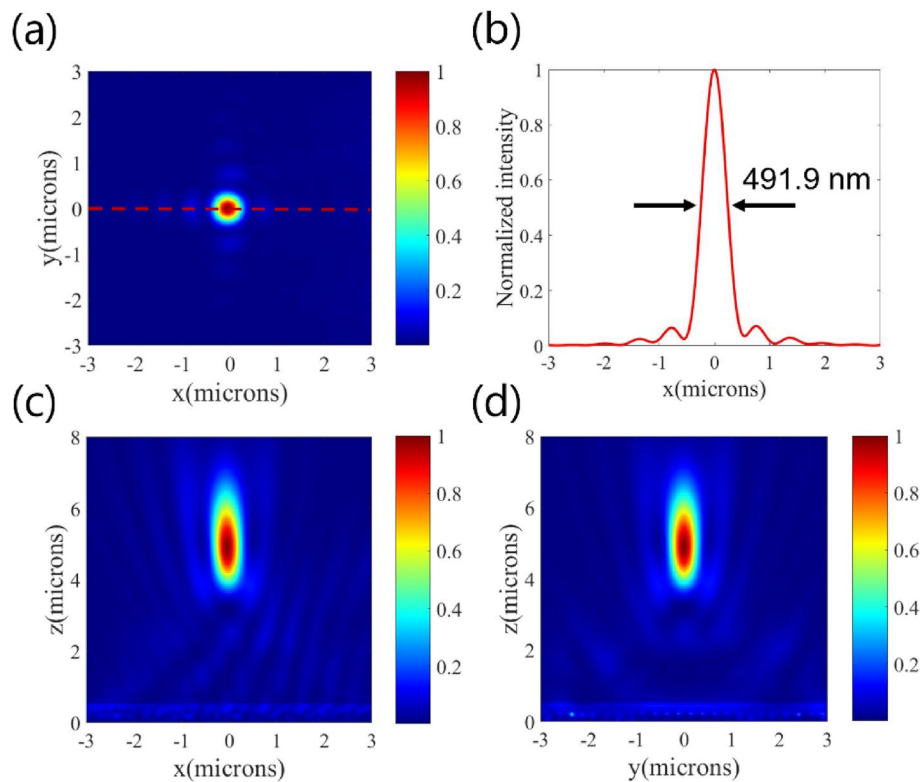


Fig. 8 Simulation results of a designed metalens with $NA=0.73$ at the illumination wavelength of 633 nm. The area of this metalens is $7.5 \times 7.5 \mu\text{m}^2$ (30×30 units), and the focal length is $5 \mu\text{m}$. **(a)** Normalized intensity profile of the metalens at the focal plane ($z = 5 \mu\text{m}$). **(b)** Corresponding normalized intensity profile along the red dashed line in **(a)**. Normalized intensity distribution in the x - z plane **(c)** and y - z plane **(d)**. The metalens is designed at λ_d and the focal length of the metalens is designed to be $5 \mu\text{m}$

to tailor phase profiles at discrete [24, 25, 34, 49] or broadband [66, 67] wavelengths. In addition, the diffraction efficiencies of green and blue light are currently lower than that of red. To balance RGB color brightness, possible solutions include using a more transparent dielectric material to reduce the absorption at the short wavelengths, or pre-adjusting the RGB brightness of the micro-display. All these techniques can be extended to our proposed device so as to carry out the design of achromatic metalens-visors in the near future.

Conclusions

We have proposed and demonstrated an optical see-through reflective metalens for AR display. It reflects 45° incident red light into a focusing point, while maintaining good transparency for white light from the other side. The crystalline silicon nanofins ensure high reflectance at the interface, and the structure of the PB phase metalens is optimized for balancing the reflective focusing efficiency and transmittance spectrum. The fabricated metalens achieves a focusing efficiency of 16.03% and a diffraction limited FWHM spot of $11.49 \mu\text{m}$ at $\lambda = 633 \text{ nm}$, and good transmission property for the normal-incident visible light covering from 400 nm to 700 nm. We further employed the metalens in an AR display system to carry out the imaging experiments of virtual images augmented

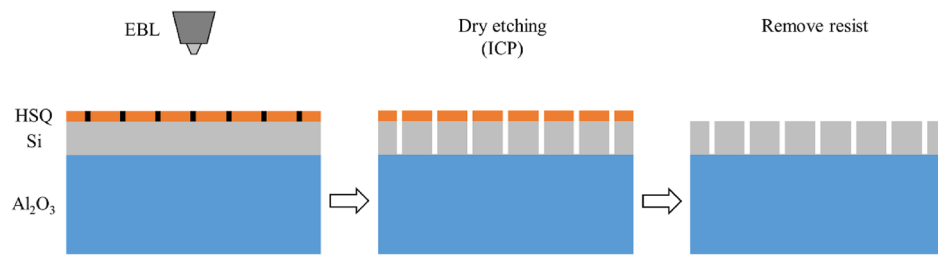


Fig. 9 Fabrication flow of the metalens-visor

on the real world. Compared to the traditional transmissive or reflective metalenses, our ultracompact multifunctional metalens visor makes the additional optical combiner needless and greatly reduces the complexity, formfactor, and weight of the near-eye AR display system. Such a metalens-visor design with the unprecedented optical characteristics would enable more versatile functionalities, and broaden the boundary of the application of metalenses in more interdisciplinary areas.

Methods

The metalens designed with a diameter of 1 mm and a focal length of 20 mm was fabricated on a crystalline silicon-on-sapphire (SOS) wafer with 230 (± 10) nm thick c-Si on 460 (± 20) μm thick sapphire. The pattern is defined in high resolution negative resist (Hydrogen silsesquioxane, HSQ, 100 nm thick film, Dow Corning) by electron beam lithography (Raith Vistec EBPG- 5000plusES) written at 100 keV. The development is performed in tetramethylammonium hydroxide, and the patterned sample is etched in an Inductively Coupled Plasma tool (ICP, Oxford Instruments PlasmaPro 100ICP180) with HBr chemistry, which has been optimized for vertical, smooth sidewalls and a high aspect ratio of the nanofins. Finally, the redundant HSQ is removed by hydrogen fluoride acid. The schematic of the fabrication flow is shown in Fig. 9.

Abbreviations

VR	Virtual reality
AR	Augmented reality
PB	Pancharatnam-Berry
Si	Silicon
CMOS	Complementary Metal Oxide Semiconductor
FDTD	Finite-difference time-domain
NA	Numerical aperture
CCD	Charge-coupled device
SLM	Spatial light modulator
LED	Light emitting diode
FOV	Field of view
LP	Linear polarizer
RCP	Right-handed circular polarizer
SEM	Scanning electron microscope
SOS	Silicon-on-sapphire
HSQ	Hydrogen silsesquioxane
EBL	Electron beam lithography
ICP	Inductively coupled plasma
PML	Perfectly Matched Layer
PEC	Perfect Electrical Conductor

Supplementary Information

The online version contains supplementary material available at <https://doi.org/10.1186/s43074-022-00075-z>.

Additional file 1 S1. Phase profile calculation. Fig. S1. Schematic of the off-axis reflection. S2. Parameter optimization. Fig. S2. Six-gray-level meta-grating-cell for simulation. The rotation angles of the nanofins range from 0 degrees to 150 degrees with a step of 30 degrees. (a) Top-view and (b) stereo-view of the meta-grating-cell. Fig. S3. Parameter optimization. The 1st order diffraction efficiencies of the reflected light (left), as the length and width of the nanofins vary while the height is fixed to be (a) 150 nm, (b) 170 nm, (c) 190 nm, (d) 200 nm, (e) 230 nm and (f) 250 nm, respectively, and the 0th order transmission spectra (right) of the meta-grating-cell, with the corresponding length \times width of each nanofin and the 1st diffraction efficiency labeled in the legends. Fig. S4. Effects of nanofin period on the optical performance of the metalens. (a) Focusing efficiency of the metalens with different periods. (b) 0th order transmission spectra of the metalens with different periods in the visible light region. S3. Parameter definition. Fig. S5. Schematic for critical parameters in the AR near-eye display system based on the reflective metalens. S4. Focusing experiments. Fig. S6. Optical setup for focusing experiments. Fig. S7. Schematic of the simulation setup for the downsized metalens with a NA of 0.035 in FDTD. Fig. S8. Focal spots of the fabricated metalens at the illumination wavelength of 633 nm. The area of the simulated metalens is $7.5 \times 7.5 \mu\text{m}^2$ (30×30 units), and the focal length is 150 μm , while the actual fabricated sample for experiment has an area of $1 \times 1 \text{mm}^2$ (4000×4000 units) and a focal length of 20 mm. (a) Measured intensity profile of the fabricated metalens at the focal plane ($z = 20$ mm). Scale bar, 20 μm . (b) Simulated intensity profile of the metalens at the focal plane ($z = 150 \mu\text{m}$). (c) Corresponding normalized intensity profiles along the dashed lines in (a) and (b) respectively. The FWHM is 11.34 μm for simulation and 11.49 μm for experiment. S5. Transmitted wavefront analysis. Fig. S9. Phase distribution of waves under the illumination wavelengths of (a) 442 nm, (b) 560 nm and (c) 646 nm, respectively, when $y = 0$. The dashed black line marks the position of the metalens-visor. The part below the dashed line shows the phase distribution of the normal incident plane wave, and the part above it shows that of the transmitted wave. S6. Monochromatic imaging experiments. Fig. S10. Optical setup for imaging experiments using a receiving screen. Fig. S11. Imaging results of the metalens using the receiving screen. The imaging depths (distances between the receiving screen and the metalens) are (a) 130 mm (dial), (b) 260 mm (puppet) and (c) 400 mm (rod labeled "R"), respectively. The virtual images are legible at all depths. Fig. S12. Sizes of images on the receiving screen. The distances between the receiving screen and the metalens are (a) 20 mm, (b) 92 mm, (c) 170 mm and (d) 250 mm. S7. Maxwellian-view display. Fig. S13. Schematic of the Maxwellian-view display. S8. Eyebow enlargement techniques. Fig. S14. Eyebow enlargement techniques. (a) Multiple viewpoints and (b) pupil duplication to enlarge the eyebow. S9. Optical setup for color imaging. Fig. S15. Optical setup for "RGB" imaging experiment with an ideal achromatic metalens. Fig. S16. Optical setup for "RGB" imaging experiment with the fabricated metalens. The incident angles of RGB wavelengths are about 0° , 6.48° and 11.34° , respectively.

Acknowledgements

The authors thank Jianghao Xiong and Kun Yin for helpful discussions. They are both from University of Central Florida.

Authors' contributions

Y. Li and Y. Su conceived the idea and initiated the project. S. Chen and Y. Li mainly wrote the manuscript and produced the Figs. S. T. Wu and Y. Ling edited the manuscript. S. Chen, X. Ren, S. Liu, H. Liang, and L. Luo contributed to the simulation and experimental results. H. Liang and S. T. Wu and Y. Su supervised the project. All authors read and approved the final manuscript.

Funding

The authors are indebted to National Key Research and Development Program (No. 2020YFC2007102), National Natural Science Foundation of China (61727808, 62075127 & 12074444), Guangdong Basic and Applied Basic Research Foundation (No. 2020A1515011184), and Guangzhou Basic and Applied Basic Research Foundation (No. 202102020987) for the financial support.

Availability of data and materials

All data needed to evaluate the conclusions in the paper are present in the paper. Additional data related to this paper may be requested from the authors.

Declarations

Competing interests

The authors declare that they have no competing interests.

Received: 15 July 2022 Revised: 1 November 2022 Accepted: 14 November 2022

Published online: 29 November 2022

References

- Xiong J, Hsiang E-L, He Z, Zhan T, Wu S-T. Augmented reality and virtual reality displays: emerging technologies and future perspectives. *Light Sci Appl*. 2021;10:216.
- Li Z, Lin P, Huang Y-W, Park J-S, Chen WT, Shi Z, et al. Meta-optics achieves RGB-achromatic focusing for virtual reality. *Sci Adv*. 2021;7:eabe4458.

3. Xiong J, Wu S-T. Planar liquid crystal polarization optics for augmented reality and virtual reality: from fundamentals to applications. *eLight*. 2021;1:3.
4. Zhan T, Xiong J, Zou J, Wu S-T. Multifocal displays: review and prospect. *Photonix*. 2020;1:10.
5. Wang D, Liu C, Shen C, Xing Y, Wang Q-H. Holographic capture and projection system of real object based on tunable zoom lens. *Photonix*. 2020;1:6.
6. Nikolov DK, Cheng F, Ding L, Bauer A, Vamivakas AN, Rolland JP. See-through reflective metasurface diffraction grating. *Opt Mater Express*. 2019;9:4070–80.
7. Grady NK, Heyes JE, Chowdhury DR, Zeng Y, Reiten MT, Azad AK, et al. Terahertz metamaterials for linear polarization conversion and anomalous refraction. *Science*. 2013;340:1304–7.
8. Wong AM, Eleftheriades GV. Perfect anomalous reflection with a bipartite Huygens' metasurface. *Phys Rev X*. 2018;8:011036.
9. Sell D, Yang J, Doshay S, Yang R, Fan JA. Large-angle, multifunctional metagratings based on freeform multimode geometries. *Nano Lett*. 2017;17:3752–7.
10. Khorasaninejad M, Zhu AY, Roques-Carmes C, Chen WT, Oh J, Mishra I, et al. Polarization-insensitive metalenses at visible wavelengths. *Nano Lett*. 2016;16:7229–34.
11. Wang Q, Zhang X, Xu Y, Tian Z, Gu J, Yue W, et al. A broadband metasurface-based terahertz flat-lens array. *Adv Opt Mater*. 2015;3:779–85.
12. Lin D, Fan P, Hasman E, Brongersma ML. Dielectric gradient metasurface optical elements. *Science*. 2014;345:298–302.
13. Wang B, Dong F, Yang D, Song Z, Xu L, Chu W, et al. Polarization-controlled color-tunable holograms with dielectric metasurfaces. *Optica*. 2017;4:1368–71.
14. Wang L, Kruk S, Tang H, Li T, Kravchenko I, Neshev DN, et al. Grayscale transparent metasurface holograms. *Optica*. 2016;3:1504–5.
15. Huang K, Dong Z, Mei S, Zhang L, Liu Y, Liu H, et al. Silicon multi-meta-holograms for the broadband visible light. *Laser Photonics Rev*. 2016;10:500–9.
16. Zhao R, Huang L, Wang Y. Recent advances in multi-dimensional metasurfaces holographic technologies. *Photonix*. 2020;1:20.
17. Zhang S, Huang L, Li X, Zhao R, Wei Q, Zhou H, et al. Dynamic display of full-stokes vectorial holography based on metasurfaces. *ACS Photonics*. 2021;8:1746–53.
18. Wei Q, Sain B, Wang Y, Reineke B, Li X, Huang L, et al. Simultaneous spectral and spatial modulation for color printing and holography using all-dielectric metasurfaces. *Nano Lett*. 2019;19:8964–71.
19. Zhao R, Sain B, Wei Q, Tang C, Li X, Weiss T, et al. Multichannel vectorial holographic display and encryption. *Light Sci Appl*. 2018;7:95.
20. Genevet P, Yu N, Aieta F, Lin J, Kats MA, Blanchard R, et al. Ultra-thin plasmonic optical vortex plate based on phase discontinuities. *Appl Phys Lett*. 2012;100:013101.
21. Luo W, Sun S, Xu H-X, He Q, Zhou L. Transmissive ultrathin Pancharatnam-Berry metasurfaces with nearly 100% efficiency. *Phys Rev Appl*. 2017;7:044033.
22. Sun J, Wang X, Xu T, Kudyshev ZA, Cartwright AN, Litchinitser NM. Spinning light on the nanoscale. *Nano Lett*. 2014;14:2726–9.
23. Avayu O, Almeida E, Prior Y, Ellenbogen T. Composite functional metasurfaces for multispectral achromatic optics. *Nat Commun*. 2017;8:14992.
24. Lee G-Y, Hong J-Y, Hwang S, Moon S, Kang H, Jeon S, et al. Metasurface eyepiece for augmented reality. *Nat Commun*. 2018;9:4562.
25. Fan Z-B, Qiu H-Y, Zhang H-L, Pang X-N, Zhou L-D, Liu L, et al. A broadband achromatic metalens array for integral imaging in the visible. *Light Sci Appl*. 2019;8:67.
26. Khorasaninejad M, Chen WT, Devlin RC, Oh J, Zhu AY, Capasso F. Metalenses at visible wavelengths: diffraction-limited focusing and subwavelength resolution imaging. *Science*. 2016;352:1190–4.
27. Zou X, Zheng G, Yuan Q, Zang W, Chen R, Li T, et al. Imaging based on metalenses. *Photonix*. 2020;1:2.
28. Wang S, Wu PC, Su V-C, Lai Y-C, Chen M-K, Kuo HY, et al. A broadband achromatic metalens in the visible. *Nat Nanotechnol*. 2018;13:227–32.
29. Anker JN, Hall WP, Lyandres O, Shah NC, Zhao J, Van Duyne RP. Biosensing with plasmonic nanosensors. *Nat Mater*. 2008;7:442–53.
30. Khorasaninejad M, Chen W-T, Oh J, Capasso F. Super-dispersive off-axis meta-lenses for compact high resolution spectroscopy. *Nano Lett*. 2016;16:3732–7.
31. Zhu AY, Chen W-T, Khorasaninejad M, Oh J, Zaidi A, Mishra I, et al. Ultra-compact visible chiral spectrometer with metalenses. *APL Photonics*. 2017;2:036103.
32. Tseng ML, Hsiao HH, Chu CH, Chen MK, Sun G, Liu AQ, et al. Metalenses: advances and applications. *Adv Opt Mater*. 2018;6:1800554.
33. Wang C, Yu Z, Zhang Q, Sun Y, Tao C, Wu F, et al. Metalens eyepiece for 3D holographic near-eye display. *Nanomaterials*. 2021;11:1920.
34. Li Z, Pestourie R, Park J-S, Huang Y-W, Johnson SG, Capasso F. Inverse design enables large-scale high-performance meta-optics reshaping virtual reality. *Nat Commun*. 2022;13:2409.
35. Hong C, Colburn S, Majumdar A. Flat metaform near-eye visor. *Appl Opt*. 2017;56:8822–7.
36. Bayati E, Wolfram A, Colburn S, Huang L, Majumdar A. Design of achromatic augmented reality visors based on composite metasurfaces. *Appl Opt*. 2021;60:844–50.
37. Avayu O, Ditcovski R, Ellenbogen T. Ultrathin full color visor with large field of view based on multilayered metasurface design. *Proc SPIE Int Soc Opt Photonics*. 2018;10676:1067612.
38. Nikolov DK, Bauer A, Cheng F, Kato H, Vamivakas AN, Rolland JP. Metaform optics: bridging nanophotonics and freeform optics. *Sci Adv*. 2021;7:eabe5112.
39. Song J-H, van de Groep J, Kim SJ, Brongersma ML. Non-local metasurfaces for spectrally decoupled wavefront manipulation and eye tracking. *Nat Nanotechnol*. 2021;16:1224–30.
40. Pancharatnam S. Generalized theory of interference and its applications. *Proc Indian Acad Sci Sect A*. 1956;44:398–417.

41. Berry MV. The adiabatic phase and Pancharatnam's phase for polarized light. *J Mod Opt.* 1987;34:1401–7.
42. Liang H, Lin Q, Xie X, Sun Q, Wang Y, Zhou L, et al. Ultrahigh numerical aperture metalens at visible wavelengths. *Nano Lett.* 2018;18:4460–6.
43. Aieta F, Kats MA, Genevet P, Capasso F. Multiwavelength achromatic metasurfaces by dispersive phase compensation. *Science.* 2015;347:1342–5.
44. Shrestha S, Overvig AC, Lu M, Stein A, Yu N. Broadband achromatic dielectric metalenses. *Light Sci Appl.* 2018;7:85.
45. Zhou Z, Li J, Su R, Yao B, Fang H, Li K, et al. Efficient silicon metasurfaces for visible light. *ACS Photonics.* 2017;4:544–51.
46. Sun Q, Liang H, Zhang J, Feng W, Martins ER, Krauss TF, et al. Highly efficient air-mode silicon Metasurfaces for visible light operation embedded in a protective silica layer. *Adv Opt Mater.* 2021;9:2002209.
47. Chen WT, Zhu AY, Capasso F. Flat optics with dispersion-engineered metasurfaces. *Nat Rev Mater.* 2020;5:604–20.
48. Sell D, Yang J, Doshay S, Zhang K, Fan JA. Visible light metasurfaces based on single-crystal silicon. *ACS Photonics.* 2016;3:1919–25.
49. Feng W, Zhang J, Wu Q, Martins A, Sun Q, Liu Z, et al. RGB achromatic Metalens doublet for digital imaging. *Nano Lett.* 2022;22:3969–75.
50. Cheng D, Wang Q, Liu Y, Chen H, Ni D, Wang X, et al. Design and manufacture AR head-mounted displays: a review and outlook. *Light Adv Manuf.* 2021;2:350–69.
51. Jang C, Bang K, Moon S, Kim J, Lee S, Lee B. Retinal 3D: augmented reality near-eye display via pupil-tracked light field projection on retina. *ACM Trans Graph.* 2017;36:190.
52. Westheimer G. The maxwellian view. *Vis Res.* 1966;6:669–82.
53. Hua H. Enabling focus cues in head-mounted displays. *Proc IEEE.* 2017;105:805–24.
54. Takaki Y, Fujimoto N. Flexible retinal image formation by holographic Maxwellian-view display. *Opt Express.* 2018;26:22985–99.
55. Zhou P, Li Y, Liu S, Su Y. Compact design for optical-see-through holographic displays employing holographic optical elements. *Opt Express.* 2018;26:22866–76.
56. Li G, Lee D, Jeong Y, Cho J, Lee B. Holographic display for see-through augmented reality using mirror-lens holographic optical element. *Opt Lett.* 2016;41:2486–9.
57. Hua J, Hua E, Zhou F, Shi J, Wang C, Duan H, et al. Foveated glasses-free 3D display with ultrawide field of view via a large-scale 2D-metagrating complex. *Light Sci Appl.* 2021;10:213.
58. Wang L, Li Y, Liu S, Su Y, Teng D. Large depth of range Maxwellian-viewing SMV near-eye display based on a Pancharatnam-Berry optical element. *IEEE Photonics J.* 2021;14:7001607.
59. Liu S, Li Y, Zhou P, Chen Q, Li S, Liu Y, et al. Full-color multi-plane optical see-through head-mounted display for augmented reality applications. *J Soc Inf Disp.* 2018;26:687–93.
60. Chen Q, Peng Z, Li Y, Liu S, Zhou P, Gu J, et al. Multi-plane augmented reality display based on cholesteric liquid crystal reflective films. *Opt Express.* 2019;27:12039–47.
61. Kim S-B, Park J-H. Optical see-through Maxwellian near-to-eye display with an enlarged eyepiece. *Opt Lett.* 2018;43:767–70.
62. Lin T, Zhan T, Zou J, Fan F, Wu S-T. Maxwellian near-eye display with an expanded eyepiece. *Opt Express.* 2020;28:38616–25.
63. Park J-S, Zhang S, She A, Chen WT, Lin P, Yousef KM, et al. All-glass, large metalens at visible wavelength using deep-ultraviolet projection lithography. *Nano Lett.* 2019;19:8673–82.
64. Zhan T, Zou J, Xiong J, Liu X, Chen H, Yang J, et al. Practical chromatic aberration correction in virtual reality displays enabled by cost-effective ultra-broadband liquid crystal polymer lenses. *Adv Opt Mater.* 2020;8:1901360.
65. Chen WT, Zhu AY, Sanjeev V, Khorasaninejad M, Shi Z, Lee E, et al. A broadband achromatic metalens for focusing and imaging in the visible. *Nat Nanotechnol.* 2018;13:220–6.
66. Hsiao HH, Chen YH, Lin RJ, Wu PC, Wang S, Chen BH, et al. Integrated resonant unit of metasurfaces for broadband efficiency and phase manipulation. *Adv Opt Mater.* 2018;6:1800031.
67. Wang S, Wu PC, Su V-C, Lai Y-C, Hung Chu C, Chen J-W, et al. Broadband achromatic optical metasurface devices. *Nat Commun.* 2017;8:187.

Publisher's Note

Springer Nature remains neutral with regard to jurisdictional claims in published maps and institutional affiliations.

Submit your manuscript to a SpringerOpen® journal and benefit from:

- Convenient online submission
- Rigorous peer review
- Open access: articles freely available online
- High visibility within the field
- Retaining the copyright to your article

Submit your next manuscript at ► [springeropen.com](https://www.springeropen.com)
